

Learned Multi-View Texture Super-Resolution

Audrey Richard¹, Ian Cherabier¹, Martin R. Oswald¹,
Vagia Tsiminaki^{*2}, Marc Pollefeys^{1,3} and Konrad Schindler¹

¹ETH Zurich, ²IBM Research Zurich, ³Microsoft Zurich

Abstract

We present a super-resolution method capable of creating a high-resolution texture map for a virtual 3D object from a set of lower-resolution images of that object. Our architecture unifies the concepts of (i) multi-view super-resolution based on the redundancy of overlapping views and (ii) single-view super-resolution based on a learned prior of high-resolution (HR) image structure. The principle of multi-view super-resolution is to invert the image formation process and recover the latent HR texture from multiple lower-resolution projections. We map that inverse problem into a block of suitably designed neural network layers, and combine it with a standard encoder-decoder network for learned single-image super-resolution. Wiring the image formation model into the network avoids having to learn perspective mapping from textures to images, and elegantly handles a varying number of input views. Experiments demonstrate that the combination of multi-view observations and learned prior yields improved texture maps.

1. Introduction

Capturing virtual 3D object models is one of the fundamental tasks of computer vision. Movies, computer games, and all sorts of future virtual and augmented reality applications require methods to create visually realistic 3D content. Besides reconstructing the best possible 3D geometry, an equally important, but perhaps less appreciated step of that modeling process is to generate high-fidelity surface texture. However, the vast majority of image-based 3D reconstruction methods ignores the texture component and merely stitches or blends pieces of the input images to a texture map in a post-processing step, at the resolution of the inputs, e.g., [8, 4, 11, 58].

Here, we explore the possibility to compute a *higher resolution texture map*, given a set of images with known camera poses that observe the same 3D object, and a 3D surface mesh of the object (which may or may not have been created

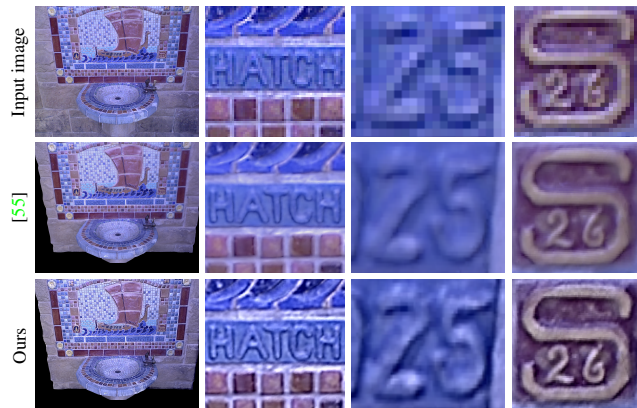


Figure 1. Learned super-resolution result compared to the state-of-the-art (upscaling $\times 4$). The result of our learning-based multi-view method is significantly sharper than prior art [55].

from those images). We argue that sticking to the original resolution actually under-exploits the image information: it is well established in the literature that, under reasonable conditions, super-resolution (SR) by a factor of at least $\times 2$ to $\times 4$ is feasible. Figure 1 shows an example of our method that illustrates this task.

There are two fundamentally different approaches to image super-resolution: (i) *redundancy-based multi-image SR*, which uses the fact that each camera view represents a different spatial sampling of the same object surface. The resulting oversampling can be used to reconstruct the underlying surface reflectance at higher resolution in a physically consistent manner, by inverting the image formation process that mapped the surface to the different views. On the other hand, (ii) *prior-based single-image SR* aims to generate a plausible, visually convincing high-resolution (HR) image from a single low-resolution (LR) image, by learning from examples what HR patterns are likely to have produced the low-resolution image content. Also for this obviously ill-posed problem, impressive visual quality has been achieved, particularly with recent deep learning approaches. Clearly, single-image SR can only ever “hallucinate from memory”, since it is entirely based on prior knowledge. There is no redundancy to constrain the reconstructed high-frequency content to be physically correct. In our classi-

*This work has been done while the author was at ETH Zurich.

fication prior-based methods include recent learning-based single-image SR techniques, but also techniques not based on learning, *e.g.*, exemplar-based ones. Historically, the prior on the output image has often been handcrafted, while today it is mostly learned from training data.

Each of the two approaches has been shown – separately – to work rather well on natural images. But the vast majority of existing work is limited to either one or the other. Our goal in this paper is to unify them both into an integrated computational model that combines their respective advantages. Moreover, our model can learn to rely more on one or the other paradigm, depending on the available data. To our knowledge our work is the first such integrated model for the general multi-view setting.

In summary, the contributions of the present paper are: (i) the first super-resolution framework capable of combining, in a general multi-view setting, redundancy-based multi-view SR with single-image SR based on a learned HR image prior. (ii) A network architecture that merges state-of-the-art deep learning and traditional variational SR methods. This unifying architecture has multiple advantages: (i) it seamlessly handles an arbitrary number of input images, and is invariant to their ordering; including the special case of a single image (falling back to pure single-view SR).

(ii) It does not waste resources, potentially sacrificing robustness, to learn known operations such as perspective projection to relate images taken from different viewpoints. (iii) It focusses the learning effort on small residual corrections, in both the single- and multi-view branches, thus reducing the amount of training data needed.

2. Related Work

In the following we focus on the most related works and group them according to the problem setting. We differentiate between the two very different paradigms of *prior-based single-image SR* and *redundancy-based multi-image SR*.

Prior-based Single-image SR. The goal of single-image SR is to fill in HR image patterns by leveraging a prior derived either from similar patches in other parts of the input image (self-exemplars) [14, 21], or from similar image patches from an existing image database [13], or – most commonly – from previously seen training data [25, 48, 53, 54]. Recently the technologies of choice for learning the prior have been (deep) convolutional networks [10, 64, 46, 22, 66, 49] and generative adversarial networks [31, 60, 42, 61, 59]. An overview of recent single-image SR methods is given in the report of the NTIRE Challenge [3]. Further surveys can be found in [18, 65, 62]. Single-view SR has also been applied to the 3D setting, for the special case of face reconstruction, to generate both texture maps [45] and displacement maps [23].

Single-image SR methods upsample to some “educated guess”. They inpaint/hallucinate high-frequency informa-

tion that is *plausible* according to previously seen examples, but they intrinsically cannot distinguish between the true HR image and another plausible candidate.

Redundancy-based Multi-image SR. In contrast to single-image SR, multi-image SR recovers high-frequency details from the redundant observations afforded by multiple images that depict the same scene. The crucial condition (which luckily is easier to meet than to violate in practice) is that each image is captured with a small, sub-pixel offset relative to all others, so that the surface is oversampled.

Multi-frame (including video) SR methods have been tackled with a Bayesian model [37], with variational methods [39, 56], and with deep learning [35, 51, 47, 24]. Also hybrid methods have been developed that build on the variational approach, but learn the regularization [27]. In contrast to the multi-view setting considered in the present paper, all these works require very small view point changes as well as a fixed number of input frames.

Multi-view Texture Mapping. In order to compute the color of a surface point visible in multiple images, one can either try to select the best view or blend multiple views. Blending can in the simplest case mean averaging, typically weighted according to visibility and surface viewing angle [8]. To avoid over-smoothed textures, blur and ghosting artifacts, several authors have introduced additional texture registration steps [33, 4, 52, 11, 58]. Rather than blending multiple images, only one image was used in [32] as texture at any given location followed by a MRF model to avoid artifacts at seams. A recurrent issue for texture generation is misregistration due to inaccurate 3D geometry and/or camera calibration. One can try to improve the geometry during texture mapping [50] for better texture quality. A more common strategy is to estimate a generic 2D optical flow field per image that compensates small registration errors [11, 58]. Overall, the goal of these methods is to prevent degradations during texturing, their upper bound is the quality of an individual source image. Texture SR aims to exceed the quality of individual input images.

Multi-view Texture SR. Early work [29] suggested to create textures with a resolution higher than the input images through oversampling. The seminal work [16] was perhaps the first that really super-resolved texture maps. That line of work was later extended to also refine surface geometry [17] and camera calibration [15]. Also here, it was shown that calibration and geometry errors can be compensated more effectively with the help of optical flow [55]. In [9], the authors focus on surface refinement, but also perform texture super-resolution, with a simple bilinear kernel.

An interesting, albeit computationally demanding alternative is to implicitly super-resolve the texture by reconstructing surface elements with constant colour, but very high-resolution, as in [38]. There abundant RGB-D data is integrated into a HR voxel model. With very accurate

geometry and calibration, texture can then be computed by simple color blending per surface voxel.

All these works exploit view redundancy, while ignoring the possibility to learn an a-priori model of HR image statistics, as learning-based single-view methods do.

Multi-view Learning-based Texture SR. Only recently, deep learning-based methods have been introduced in the multi-view case to enhance the quality of the reconstructed models, *e.g.*, for facial scans [40]. For facial animation a deep generative network to infer per-frame texture deformation was introduced [41]. In the context of cloth simulation one can compute a global shape deformation and generate high-frequency normal maps with a GAN [30]. Recently, per-image SR was extended to the multi-view case, by injecting the 3D information in the form of normal maps [34], reaching similar performance as 3D model-based methods.

The latter works leverage the capacity of deep neural networks, yet a method that explicitly incorporates both model-based and learning-based techniques is still missing. In this paper, we construct such a method, by converting the model-based pipeline into a neural network architecture and merging it with conventional, learned single-image SR.

3. Method

Overview. The inputs to our method are a set of calibrated LR images and a 3D surface given by a mesh. Its output is a SR texture atlas that can be directly used for 3D rendering.

Using the calibrated LR images, we estimate an initial (still blurry) texture atlas. The way the texture atlas is created is arbitrary. We then use a neural network architecture consisting of two major parts to super-resolve the texture atlas. The *redundancy-based* part aggregates multi-view redundancy from all LR input images and computes an intermediate, super-resolved texture atlas. The *prior-based* part enhances the single, intermediate atlas using knowledge about its expected statistics that it has collected from a training dataset. We refer to the former as Multi-View Aggregation (MVA) subnet, and the latter as Single-Image Prior (SIP) subnet. The overall network architecture with the two sub-networks is shown in Figure 2 and the individual parts are detailed in the following subsections.

3.1. Multi-View Aggregation (MVA)

The goal of MVA is to generate a super-resolved texture atlas by leveraging multi-view redundancy. The corresponding network branch is shown in the blue box of Figure 2. It exploits the image formation model to explicitly define the texture-to-input correspondence via projections.

Motivation. In a multi-view setting the number of views that are useful for reconstructing the texture at a particular surface point varies, as it depends on the camera setup and the surface geometry (including self-occlusions). To

deal with varying number of inputs, deep networks typically use pooling [43, 2] or recurrent architectures (*e.g.*, LSTMs [20]). We argue that none of them is well-suited for redundancy-based SR: the *average pooling* operation blurs multiple inputs into a single value, which is counter-productive when aiming to recover HR information. *Max-pooling* selects only a single input, discarding multi-view information – information mixed by integration cannot be recovered by selection. As for *recurrent networks*, their result depends on the order in which the images are processed, which contradicts common sense (and the image formation model). Instead, we propose to incorporate the (inverse) image formation model into the network in the form of special layers that perform redundancy-based multi-image SR. By explicitly modeling blurring and downsampling, one can relate any number of LR input views to the desired HR output.

Notation. We are given a set of N LR images $\{I_i\}_{i=1}^N$, with $I_i: \Omega_i \subset \mathbb{R}^2 \rightarrow \mathbb{R}$ (grayscale). The scene geometry is provided as a mesh \mathcal{M} . For each LR image, we precompute a projection matrix that maps the texture domain to the image domain through \mathcal{M} via $P_i: \mathbb{R}^2 \rightarrow \mathbb{R}^2$, following [55]. The output SR texture atlas is denoted $T: \mathbb{T} \subset \mathbb{R}^2 \rightarrow \mathbb{R}$.

Image Formation Model. Each input image depicts the same 3D geometry from a different viewpoint, leading to a different sampling of the surface. Together, they oversample the surface, which makes it possible to reconstruct its reflected color at higher resolution. In order to recover that HR signal, we aim to invert the image formation process. Namely, the camera lens blurs the incoming bundle of rays, and the sensor integrates (averages) the contribution of all incoming photons within a pixel. Following [12], we have:

$$I_i = DK_i W_i P_i \cdot T + e_i \quad (1)$$

An LR input image I_i is generated from the SR texture T via a sequence of perspective projection P_i , blurring with convolution kernel K_i , downsampling with operator D and adding noise e_i . The additional warp operator W_i accounts for geometric inaccuracies and camera calibration errors with an optical flow correction, precomputed as in [58, 55].

SR Multi-view Energy. Similar to [17, 55] we compute an SR texture atlas T as a minimizer of the following energy:

$$\underset{T}{\text{minimize}} \sum_{i=1}^N \|DK_i W_i P_i \cdot T - I_i\|_1 + \|g \cdot \nabla T\|_1 \quad (2)$$

The energy minimizes the re-projection error between the SR texture atlas and all inputs $\{I_i\}_{i=1}^N$. The second term is the weighted total variation regularizer, with g a locally-adaptive weight function. It favors a piecewise constant solution if the input data is ambiguous or absent and is necessary to make the optimization well-posed.

Parameter Estimation. In contrast to classical SR approaches [16, 55] for which g is manually set to some con-

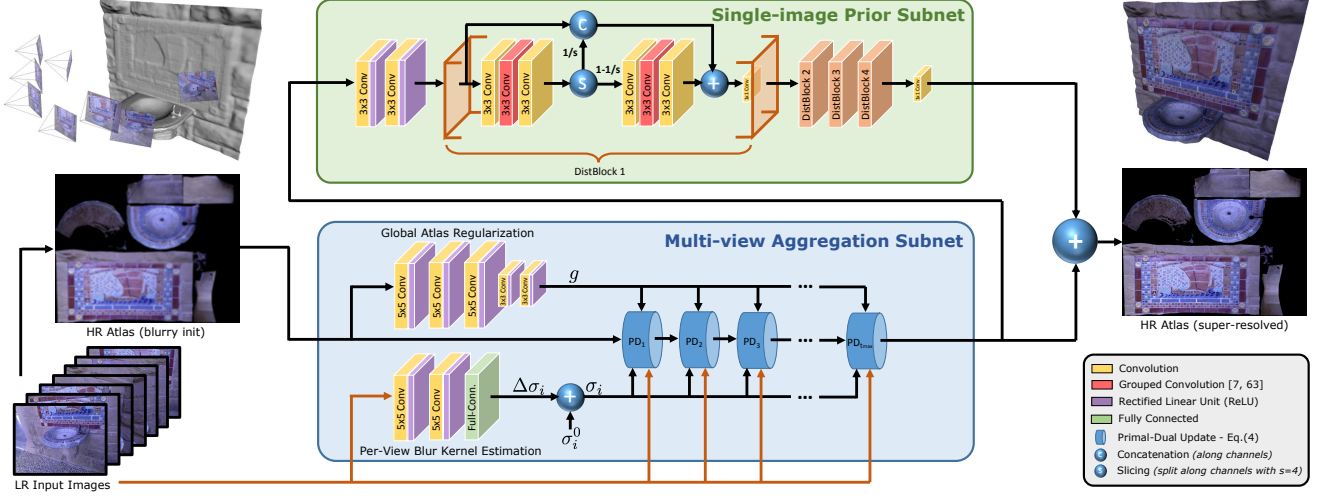


Figure 2. The proposed multi-view super-resolution network combines the concepts of *redundancy-based multi-view SR* (blue) and *prior-based single-image SR* (green) in a single end-to-end trainable architecture. The *multi-view aggregation (MVA) subnet* leverages the view redundancy to construct an intermediate SR texture atlas. The *single-image prior (SIP) subnet* learns the differences between this atlas and the ground truth to further boost the SR performance.

stant, we locally estimate the amount of smoothing from the texture atlas with a CNN, such that it yields the optimal SR reconstruction. Similarly, another small network adjusts the standard deviation σ_i of the Gaussian blur kernel K_i for each view i . See Figure 2 (left side of blue box).

MVA Layers. For numerical optimization of (2) we employ a first-order primal-dual method [5], known to be a particularly suitable solver for this type of problems. To that end, the dual variables ϕ, ξ are introduced via the Legendre-Fenchel transform of the regularizer, in order to deal with the non-differentiability of the L^1 -norm. This transforms (2) into the following saddle-point problem:

$$\min_{\mathbf{T}} \max_{\substack{\|\phi_i\|_{\infty} \leq 1 \\ \|\xi\|_{\infty} \leq 1}} \sum_{i=1}^N \langle \mathbf{D}K_i \mathbf{W}_i \mathbf{P}_i \cdot \mathbf{T} - \mathbf{I}_i, \phi_i \rangle + \langle \mathbf{g} \cdot \nabla \mathbf{T}, \xi \rangle \quad (3)$$

The algorithm in [5] jointly performs a gradient descent in the primal variable \mathbf{T} and a gradient ascent in the dual variables ϕ_i, ξ and iterates $t \in \{1, \dots, t_{\max}\}$ steps as follows:

$$\phi_i^{t+1} = \Pi_{\|\cdot\| \leq 1} [\phi_i^t + \eta (\mathbf{D}K_i \mathbf{W}_i \mathbf{P}_i \bar{\mathbf{T}}^t - \mathbf{I}_i)] \quad (4a)$$

$$\xi^{t+1} = \Pi_{\|\cdot\| \leq 1} [\xi^t + \eta \cdot \mathbf{g} \cdot \nabla \bar{\mathbf{T}}^t] \quad (4b)$$

$$\mathbf{T}^{t+1} = \mathbf{T}^t + \tau (\mathbf{g} \cdot \text{div} \xi^{t+1} - \sum_{i=1}^N \mathbf{P}_i^T \mathbf{W}_i^T \mathbf{K}_i^T \mathbf{D}^T \phi_i^{t+1}) \quad (4c)$$

$$\bar{\mathbf{T}}^{t+1} = 2\mathbf{T}^{t+1} - \mathbf{T}^t \quad (4d)$$

where $\eta = \tau = 0.025$ are step sizes and $\Pi_{\|\cdot\| \leq 1}$ a projection onto the L^2 unit ball per pixel. Details can be found in the *Supplementary Material*. In order to transform the numerical minimization into a neural network, we unroll a fixed

number of t_{\max} optimization steps, such that each update cycle (4) represents one network layer in our MVA subnet. Unrolling is a generic technique to include iterative energy minimization into neural network blocks, used also in low-level vision [57], medical image reconstruction [28], single image depth super-resolution [44], and semantic 3D reconstruction [6]. It allows us to combine the classical multi-view SR with learning-based single-view SR methods. The updates (4) are matrix operations and can be regarded as specifically tailored convolutions that allow the multi-view aggregation. The steps are depicted as blue cylinders in Figure 2, where each layer PD_i represents a single primal-dual update (4). The SR texture atlas estimated from multiple views is then fed into the subsequent SIP subnet.

3.2. Single-Image Prior (SIP)

The goal of the SIP subnet is to learn which high-frequency texture statistics typically underlie a given low-frequency pattern. Following recent single-image SR [22], we build our network in a way that the image prior is learned as a residual correction to the input image, since these high-frequency differences are easier to regress than the full image content. However, instead of generic (bilinear or bicubic) upsampling, we can already provide the prediction of redundancy-based MVA as input. For learning the residual prior, we follow the approach of the information distillation network [22], which exhibits a simple feed-forward network structure that also learns residual changes in composition with standard bicubic upsampling. This state-of-the-art single-image SR architecture is simple and lightweight and can easily be adapted to be combined with our MVA network (see Section 4.2). The SIP subnet is depicted in the

green box of Figure 2.

Note on Prior-based SR Correctness. The result of prior-based SR can only be *plausible*, but effectively is hallucination based entirely on *other* images. This may be undesired for applications in which correctness is more important than visual quality. Such scenarios, by definition, rule out single-frame SR. In contrast, our MVA network can also be used without the SIP part, and will likely outperform the classical energy minimization it is based on, due to its ability to learn the algorithm (meta-)parameters from data.

3.3. Loss Function

The overall network, as depicted in Figure 2, is trained in a supervised fashion. Our main training objective is the L^1 -norm of the intensity differences between the predicted texture atlas \hat{T} and the corresponding ground truth T . A second loss term is added that keeps the standard deviation σ_i of the blur kernel K_i near the initial value σ_i^0 :

$$\mathcal{L} = \|T - \hat{T}\|_1 + \alpha \cdot \sum_i \|\sigma_i - \sigma_i^0\|_2 \quad (5)$$

where $\alpha = 1$ scales the contribution of the two terms. Since the weighted TV-regularizer is defined on the texture gradient ∇T , predicting the weight function g is accounted for in the first term and a dedicated loss is not needed.

4. Experiments

4.1. Datasets

We use the following two datasets of different types:

- **Single-image DIV2K dataset [1]**: composed of 800 diverse 2K resolution high-quality natural images. The corresponding LR images $\times 2$ and $\times 4$ have been obtained synthetically using *undisclosed* degradation operators.
- **Multi-view 3D dataset:** following [16, 15, 55] we use 8 scenes (*i.e.*, *Beethoven*, *Bird*, *Bunny*, *Fountain*, *Buddha*, *Head*, *Relief*, *Temple Ring*) including calibrated LR images, appearance projections, and 3D geometry.

We convert all data into YCbCr color space and only process the Y-channel, which contains practically all high-frequency information. We use bicubic upsampling of the CbCr-channels to reconstruct the super-resolved RGB output. The DIV2K dataset is only used to pre-train the SIP subnet. Contrary to single-image SR of natural images, our method requires a precomputed texture mask to delimit the different charts. To increase the amount of data we perform data augmentation: (i) rotations with an angle of 90° , 180° , 270° , (ii) horizontal and vertical flips, (iii) four random multiplicative brightness changes with random offsets. To deal with uninformative background in texture maps, we dilate the textured regions, such that the receptive field for a

valid texture pixel contains no background. Our main multi-view 3D dataset is then split into mutually exclusive testing (*Beethoven*, *Bird*, *Bunny*) and training scenes (all others).

4.2. Implementation Details

Patch-based Approach. Working with real multi-view 3D data in combination with a neural network makes the implementation more challenging. In order to handle the massive quantity of data, mostly due to the presence of the projections P_i and the optical flows W_i , we adopt a *patch-based approach* during training. Input atlases and their corresponding super-resolved ground truths are cut into patches of size 64×64 . For every texture patch, we generate a corresponding patch in the image domain, with a size of 200×200 to ensure the reprojection falls completely inside the patch in spite of possible projective distortions - as well as the corresponding optical flow. Accordingly, the LR input images are divided into patches of size 100×100 (or 50×50) in order to train for an upsampling factor $\times 2$ (or $\times 4$).

MVA Subnet. During training, we limit the maximum number of LR views to $N = 20$. While conceptually an arbitrary number is possible, having the same number greatly simplifies batch processing. We thus only use 20 views, the minimum number available for any scene in the multi-view dataset. The selected views fully cover each object, with the best possible overlap for multi-view SR. To obtain an initial atlas (not yet super-resolved), we follow [55] and compute visibility masks from texture to image domain. They are used to generate the projection operators, as well as the initial atlas averaged from corresponding visible input views. We precomputed the optical flow using [36]¹.

SIP Subnet. Following [22], the SIP subnet is composed of 31 layers overall. Two 3×3 convolutional layers are first used to extract feature maps from the input - in our case the output of the MVA subnet; followed by 4 distillation blocks, each consisting of an “enhancement unit” and a “compression unit”. A major difference to [22] is that our SIP subnet operates directly in the target HR space. The bicubic upsampling is replaced by a skip connection, and instead of a final reconstruction block we use a 1×1 convolution layer (see Figure 2). Unsurprisingly, we found that upsampling feature maps at the end unavoidably introduces some blurring effect, whereas doing the enhancement of high-frequency content in the target domain is more effective. We initialize all weights like [19] and all biases to zero.

4.3. Training Setup

Training was run on a GTX 1080 Ti GPU (12GB RAM). The SIP subnet is first pre-trained on DIV2K data (batch size 64), then the complete MVA+SIP network is fine-tuned end-to-end on the 3D training set. We use the Adam opti-

¹<https://github.com/pathak22/pyflow>

mizer [26] with learning rate 10^{-4} . Due to memory limitations, the batch size was set to 4 for the multi-view dataset.

Ground Truth Generation. An issue in texture SR is the lack of ground truth, *i.e.*, texture with a higher resolution than that of the input images. For each scene, we generated a pseudo-ground truth texture atlas by running our MVA L^1 primal-dual model with an upsampling factor $\times 2$ from all available views (*i.e.*, using significantly more viewpoints than for testing the complete network). Since upsampling $\times 4$ in the same way leads to visually imperfect results even with many views, we instead downsample the input views to $\times 0.5$ their original size for experiments with $\times 4$ super-resolution. We note that the ground truth data may be biased towards the MVA subnet, since it is generated with it, but for training and testing we use fewer and LR input views.

Number of Input Views. At test time, the MVA subnet can process an arbitrary number of input views. For training, it is however convenient to have a fixed number. We trained two models, one with 20 and the other with 3 input views. The purpose is to simulate two cases:

- 20 views emulate dedicated texture recording with healthy redundancy; thus favoring the MVA step.
- 3 views represent a more offhanded scenario with only few images; thus relying more on the SIP step.

Figure 3 shows examples of training patches for these two cases. For the 20-view model the MVA subnet achieves sharp super-resolution texture, but tends to exaggerate the intensity contrast, the SIP subnet corrects the overshoot while preserving the recovered details. For the 3-view model, the MVA subnet can only partially recover the fine structure, which is then further sharpened by the SIP subnet. Overall, we find that the 3-view model generalizes better. This is likely due to the fact that we had to generate our ground truth with a HR, many-view version of MVA. As a consequence, a certain bias towards MVA-type outputs is baked into the ground truth. Due to that bias, MVA trained with many views gets “too close” to the imperfect ground truth, which hampers the training of the SIP. For the rest of the paper, we run all tests with the model trained on 3 views, no matter how many input views we feed it.

Runtime. Pre-training the SIP subnet on DIV2K takes about 40 min per epoch (upsampling $\times 4$). Training time for the full MVA+SIP takes 5 min per epoch for the 3-view model, respectively 20 min per epoch for the 20-view model. At test time, super-resolving the largest texture atlas (*Fountain*) with upsampling factor $\times 4$ and 20 views takes 1 hour – other scenes and settings are proportionally faster. This is significantly faster than the most similar competing method [55], which reports 30-60 minutes *per iteration*.

4.4. Results

Our evaluation is divided into two parts. A comparison to state-of-the-art methods at the upsampling factor $\times 2$ (the

one used in most previous work) and an ablation study at a more interesting upsampling factor $\times 4$.

4.4.1 Comparison with state-of-the-art

We compare our proposed end-to-end network with the state-of-the-art multi-view texture SR techniques of Tsiminaki *et al.* [55] and of Goldlücke *et al.* [16]. We use the same three objects *Beethoven*, *Bird* and *Bunny*, with identical views and 3D models. The results for competing methods are only available at upsampling factor $\times 2$, thus we show results for that (rather moderate) super-resolution in Figure 4. We point out that, for reasons unknown to us, the dataset made available to us differs from the original one. Our version has 33, 20 and 36 views respectively for the three test objects; whereas the literature suggests that the earlier [55] had access to up to 108 views.

Our approach delivers outputs with sharper details than [55], such as the letters and eyebrows in *Beethoven*, or the feathers of the *Bird*; and without the over-sharpening artifacts of [16]. It also recovers the particularly challenging fur of the *Bunny*, although with little noticeable improvements over the pure MVA method [55]. We attribute this to the strong lighting differences between the input views of the *Bunny*. As shown in Figure 3 the SIP subnet tries to correct brightness deviations (cf. Section 4.3), which may be problematic if the brightness varies across input views.

Table 1 presents a quantitative comparison of our method with two baselines (for an upsampling factor $\times 4$): an re-implementation of [55] with the more robust L^1 -dataterm, and the original version of the single-image SR network [22]. It also shows respective performance of MVA, SIP and MVA+SIP network. We report the SSIM, PSNR and SRE². SSIM measures how well the structures are recovered, while PSNR and SRE measure the overall reconstruction error. We can observe that in general our network outputs better results than the two baselines. Looking at our MVA subnet alone, it achieves high SSIM value, *i.e.*, it recovers fine geometric structures. The subsequent SIP mainly boosts the PSNR and SRE values, lifting them significantly above prior art; corresponding to enhanced color and contrast fidelity. While SIP on its own (without MVA) is not competitive, showing its dependance on an already fairly high-quality input. See also Section 4.4.3.

4.4.2 Ablation study

We also conducted an ablation study to assess the contribution of each subnet, see Figure 5. For this experiment the textures were super-resolved with a bigger upsampling factor of $\times 4$ to challenge our method.

As expected, generating a texture atlas from LR images with a state-of-the-art atlas generator such as [58] leads to

²Signal to Reconstruction Error, measured as: $10 \log_{10} \frac{\mu_x^2}{\|\bar{x} - x\|^2/n}$, with μ_x the average of x and n the number of pixels.

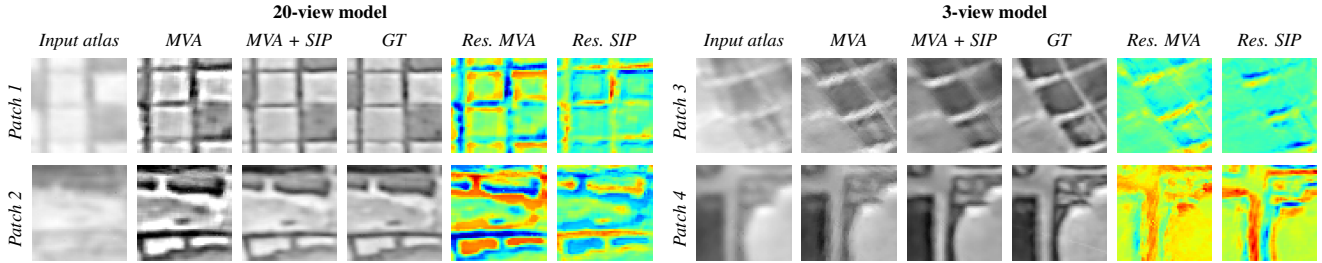


Figure 3. Texture patches at different steps of training (upsampling factor $\times 4$). Our network takes as input a patch of the initial blurry atlas. The MVA subnet outputs a super-resolved patch, which is then further refined by the SIP subnet (MVA+SIP). Patches 1 and 2 show the 20-view case, patches 3 and 4 show the 3-view case.

	Beethoven			Bird			Bunny			Average		
	SSIM	PSNR	SRE									
Tsiminaki <i>et al.</i> [55] with L^1 -dataterm	0.934	40.488	14.482	0.942	41.379	21.914	0.923	38.596	15.292	0.933	40.155	17.229
Hui <i>et al.</i> [22] (pre-trained on [1])	0.933	39.505	13.410	0.941	41.999	22.499	0.916	37.888	14.525	0.930	39.797	16.811
MVA subnet	0.931	40.260	14.253	0.944	41.901	22.436	0.922	38.573	15.268	0.933	40.245	17.319
SIP subnet (trained only on [1])	0.914	37.041	2.009	0.921	38.738	16.766	0.869	35.252	7.006	0.901	37.010	8.594
Ours (no pre-training, σ_i fixed)	0.941	39.231	13.224	0.940	39.146	19.680	0.929	38.198	14.894	0.937	38.858	15.933
Ours (SIP-Net pre-trained on [1])	0.948	43.309	17.304	0.943	44.634	25.171	0.932	39.690	16.386	0.941	42.544	19.620

Table 1. Quantitative comparison of different texture super-resolution techniques (upsampling factor $\times 4$, same initial texture atlas, all computed on the Y-channel images). The top two rows are baselines : our reimplementation of [55] with primal-dual optimization scheme and L^1 -dataterm (first row), single-image super-resolution network [22] (second row). We evaluate the individual components of our proposed approach: MVA subnet trained on our data, which is very similar to [55], but estimates the local blur from the data (third row); SIP subnet alone trained only on DIV2K (fourth row); and our complete network MVA+SIP (last two rows).

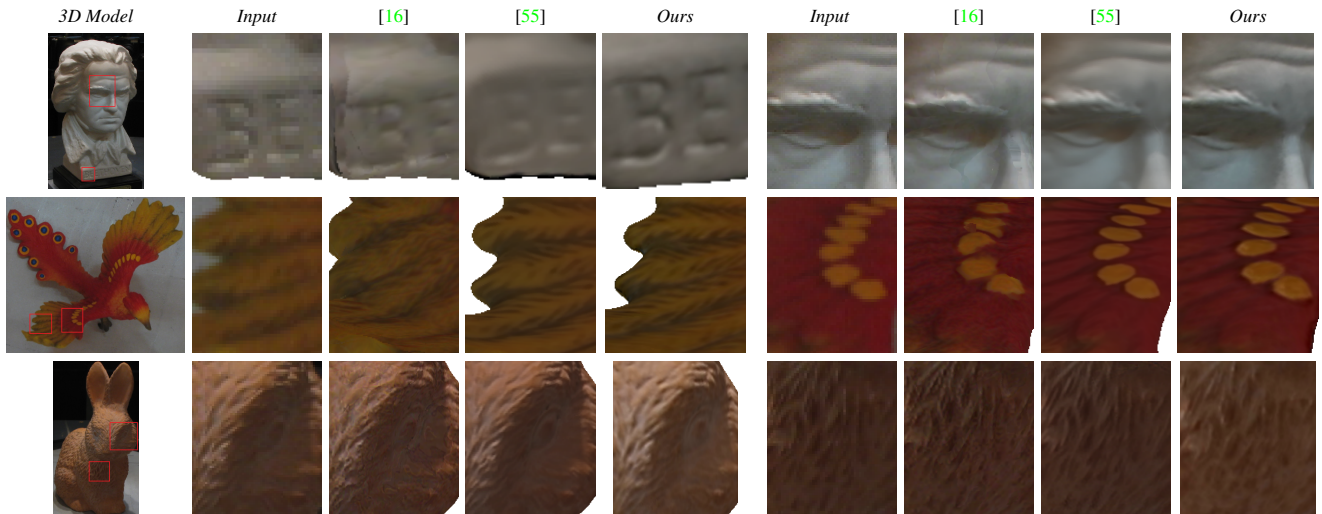


Figure 4. Qualitative comparison to state-of-the-art multi-view SR methods (upsampling factor $\times 2$). We compare to [16] and [55] for which the authors provided results for *Beethoven*, *Bird* and *Bunny* datasets (computed from 108, 52 and 52 input images, respectively). Our results were obtained with the available LR views, respectively 33, 20 and 36.

LR results. Moreover, independently super-resolving the input views and using them as input to the same generator [58] may lead to misalignments. The single-image SR method may hallucinate different high-frequency details in different views which are then hard to align. This is particularly visible on the close-ups from the *Beethoven* dataset, where the letters in "BEETHOVEN" and "S. BOCHMANN" are not correctly aligned. Leveraging the redundant information from multiple input views, the MVA

subnet can recover sharp details, such as the fur of the *Bunny*, the feathers of the *Bird*, or the letters on *Beethoven*. The SIP subnet on the other hand excels at enhancing existing details, cf. Table 1. Comparing the output of the MVA subnet with the full approach, we can see that the letters and stone texture in *Beethoven* become sharper, as does the fur around the eye of the *Bunny*. Moreover, the output of SIP without preceding MVA confirms the mentioned sensitivity of SIP to its initialization.

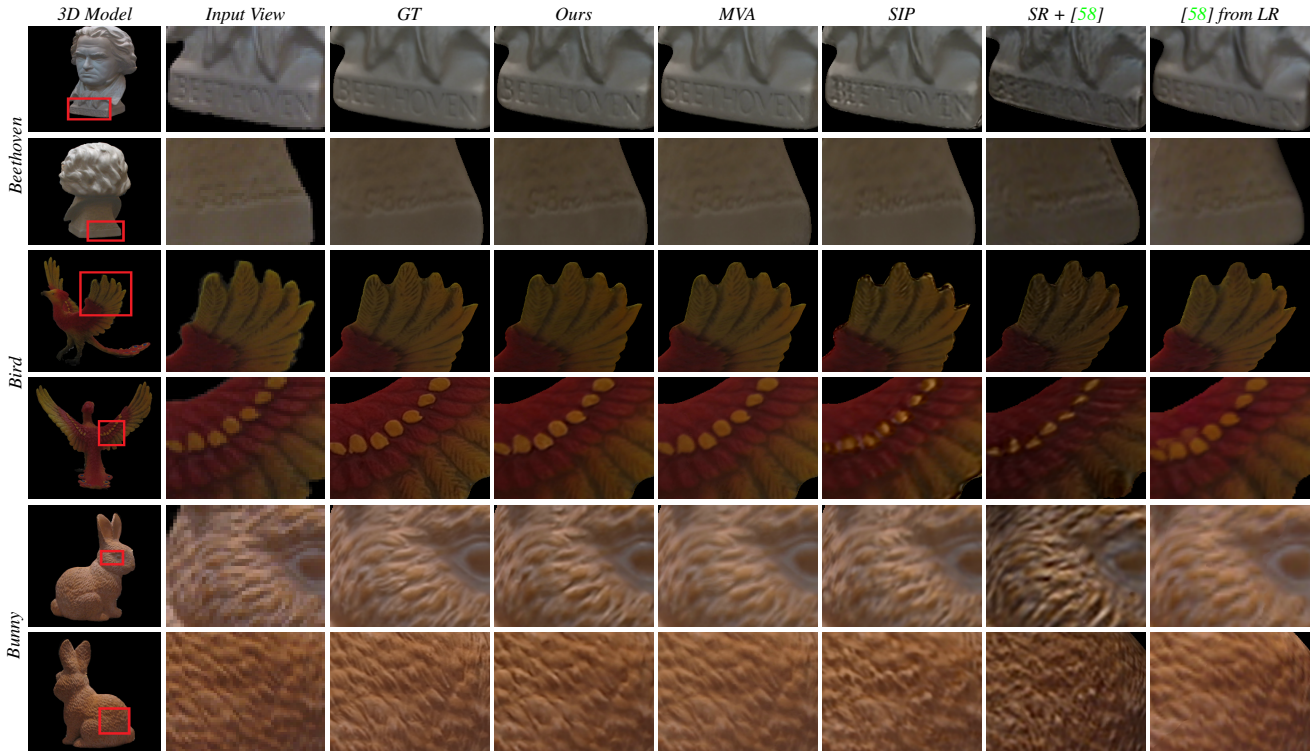


Figure 5. Ablation study and comparison (upsampling factor $\times 4$). We compare our result (fourth column) to: LR input view (second column), ground truth obtained from [55] with upsampling factor $\times 2$ from the original images (third column); output of the MVA subnet (fifth column); output of the SIP subnet without MVA (sixth column); output texture of [58] from input views super-resolved with [22] (seventh column); and output texture directly from LR input views with [58] (eighth column).

4.4.3 Discussion

Training Data. It was a challenge to find sufficient training data for our method. In particular, to train the MVA subnet one needs not only a textured 3D model, but also the projection operators P_i of the N original views used to create the texture. Due to the scarcity of such datasets, we could not afford to set aside more than three scenes (*Beethoven*, *Bird* and *Bunny*), in order to have sufficient training data. As further visual examples on some of the training scenes (*Fountain*, *Buddha* and *Relief*) in Figure 1 and in *Supplementary Material*. According to good practice in machine learning, these results were not used for quantitative evaluation.

Texture Initialization. In our experiments we found that the prior-based SIP subnet is sensitive to the quality of the LR input texture. This can be observed in Figure 5 and Table 1. If the input atlas is too blurry, e.g., due to averaging of imperfectly aligned images, then the redundancy-based MVA subnet is still able to super-resolve the patch. Whereas the SIP subnet has trouble to add further high-frequency details. On the contrary, if the input atlas already contains fine details, the MVA might not improve much, but the SIP subnet manages to further enhance them.

The MVA subnet approximates a variational optimization of a convex energy and is therefore independent of the

initialization; whereas the SIP subnet performs a small, and at most locally optimal, residual correction. Overall, the results confirm our intuition that the MVA and SIP are to some degree complementary and that their combination can achieve superior SR.

5. Conclusion

We presented a novel multi-view texture super-resolution network that unifies and exploits two fundamental approaches to super-resolution, namely physically motivated multi-view SR and prior-based single-view SR. Our end-to-end neural network design combines modern deep learning techniques with classical energy minimization methods via optimization unrolling. This leads to a problem-specific network architecture which avoids the learning of the perspective projection operator. Further, we can handle a varying number of input images and are invariant to their ordering. Several experiments demonstrate that the approach outperforms prior art in texture SR.

Acknowledgements. This research was partially supported by the Intelligence Advanced Research Projects Activity (IARPA) via Department of Interior/ Interior Business Center (DOI/IBC) contract number D17PC00280. The U.S. Government is authorized to reproduce and distribute reprints for Governmental purposes notwithstanding any copyright annotation thereon. Disclaimer: The views and conclusions contained herein are those of the authors and should not be interpreted as necessarily representing the official policies or endorsements, either expressed or implied, of IARPA, DOI/IBC, or the U.S. Government.

References

- [1] E. Agustsson and R. Timofte. NTIRE 2017 challenge on single image super-resolution: Dataset and study. In *International Conference on Computer Vision and Pattern Recognition (CVPR) Workshops*, July 2017. 5, 7
- [2] M. Aittala and F. Durand. Burst image deblurring using permutation invariant convolutional neural networks. In *European Conference on Computer Vision (ECCV)*, 2018. 3
- [3] C. Ancuti, C. O. Ancuti, R. Timofte, and et al. NTIRE 2018 challenge on image dehazing: Methods and results. In *International Conference on Computer Vision and Pattern Recognition (CVPR) Workshops*, 2018. 2
- [4] F. Bernardini, I. M. Martin, and H. E. Rushmeier. High-quality texture reconstruction from multiple scans. *IEEE Transactions on Visualization and Computer Graphics*, 7(4):318–332, 2001. 1, 2
- [5] A. Chambolle and T. Pock. A first-order primal-dual algorithm for convex problems with applications to imaging. *Journal of Mathematical Imaging and Vision*, 40(1):120–145, 2011. 4
- [6] I. Cherabier, J. L. Schönberger, M. R. Oswald, M. Pollefeys, and A. Geiger. Learning priors for semantic 3D reconstruction. In *European Conference on Computer Vision (ECCV)*, 2018. 4
- [7] F. Chollet. Xception: Deep learning with depthwise separable convolutions. In *International Conference on Computer Vision and Pattern Recognition (CVPR)*, 2017. 4
- [8] P. E. Debevec, C. J. Taylor, and J. Malik. Modeling and rendering architecture from photographs: A hybrid geometry and image-based approach. In *ACM Transactions on Graphics (Proc. SIGGRAPH)*, 1996. 1, 2
- [9] A. Delaunoy and M. Pollefeys. Photometric bundle adjustment for dense multi-view 3D modeling. In *International Conference on Computer Vision and Pattern Recognition (CVPR)*, 2014. 2
- [10] C. Dong, C. C. Loy, K. He, and X. Tang. Image super-resolution using deep convolutional networks. *IEEE Transactions on Pattern Analysis and Machine Intelligence*, 38(2):295–307, 2016. 2
- [11] M. Eisemann, B. De Decker, M. Magnor, P. Bekaert, E. de Aguiar, N. Ahmed, C. Theobalt, and A. Sellent. Floating textures. *Comp. Graph. Forum*, 27(2):409–418, 2008. 1, 2
- [12] M. Elad and A. Feuer. Super-resolution reconstruction of image sequences. *IEEE Transactions on Pattern Analysis and Machine Intelligence*, 21(9):817–834, 1999. 3
- [13] W. T. Freeman, T. R. Jones, and E. C. Pasztor. Example-based super-resolution. *IEEE Computer Graphics and Applications*, 22(2):56–65, 2002. 2
- [14] D. Glasner, S. Bagon, and M. Irani. Super-resolution from a single image. In *Proc. International Conference on Computer Vision (ICCV)*, 2009. 2
- [15] B. Goldlücke, M. Aubry, K. Kolev, and D. Cremers. A super-resolution framework for high-accuracy multiview reconstruction. *International Journal of Computer Vision*, 106(2):172–191, 2014. 2, 5
- [16] B. Goldlücke and D. Cremers. A superresolution framework for high-accuracy multiview reconstruction. In *Pattern Recognition (Proc. DAGM)*, 2009. 2, 3, 5, 6, 7
- [17] B. Goldlücke and D. Cremers. Superresolution texture maps for multiview reconstruction. In *Proc. International Conference on Computer Vision (ICCV)*, 2009. 2, 3
- [18] K. Hayat. Super-resolution via deep learning. *CoRR*, abs/1706.09077, 2017. 2
- [19] K. He, X. Zhang, S. Ren, and J. Sun. Delving deep into rectifiers: Surpassing human-level performance on imagenet classification. In *Proc. International Conference on Computer Vision (ICCV)*, 2015. 5
- [20] S. Hochreiter and J. Schmidhuber. Long short-term memory. *Neural Computation*, 9(8):1735–1780, 1997. 3
- [21] J. Huang, A. Singh, and N. Ahuja. Single image super-resolution from transformed self-exemplars. In *International Conference on Computer Vision and Pattern Recognition (CVPR)*, 2015. 2
- [22] Z. Hui, X. Wang, and X. Gao. Fast and accurate single image super-resolution via information distillation network. In *International Conference on Computer Vision and Pattern Recognition (CVPR)*, 2018. 2, 4, 5, 6, 7, 8
- [23] L. Huynh, W. Chen, S. Saito, J. Xing, K. Nagano, A. Jones, P. Debevec, and H. Li. Mesoscopic facial geometry inference using deep neural networks. In *International Conference on Computer Vision and Pattern Recognition (CVPR)*, 2018. 2
- [24] Y. Jo, S. W. Oh, J. Kang, and S. J. Kim. Deep video super-resolution network using dynamic upsampling filters without explicit motion compensation. In *International Conference on Computer Vision and Pattern Recognition (CVPR)*, 2018. 2
- [25] K. I. Kim and Y. Kwon. Single-image super-resolution using sparse regression and natural image prior. *IEEE Transactions on Pattern Analysis and Machine Intelligence*, 32:1127–1133, 2010. 2
- [26] D. P. Kingma and J. Ba. Adam: A method for stochastic optimization. *CoRR*, abs/1412.6980, 2014. 5
- [27] T. Klatzer, D. Soukup, E. Kobler, K. Hammernik, and T. Pock. Trainable regularization for multi-frame super-resolution. In *German Conference on Pattern Recognition (GCPR)*, 2017. 2
- [28] E. Kobler, T. Klatzer, K. Hammernik, and T. Pock. Variational networks: Connecting variational methods and deep learning. In *German Conference on Pattern Recognition (GCPR)*, 2017. 4
- [29] R. Koch, M. Pollefeys, and L. V. Gool. Multi viewpoint stereo from uncalibrated video sequences. In *European Conference on Computer Vision (ECCV)*, 1998. 2
- [30] Z. Löhner, D. Cremers, and T. Tung. Deepwrinkles: Accurate and realistic clothing modeling. In *European Conference on Computer Vision (ECCV)*, 2018. 3
- [31] C. Ledig, L. Theis, F. Huszar, J. Caballero, A. Cunningham, A. Acosta, A. P. Aitken, A. Tejani, J. Totz, Z. Wang, and W. Shi. Photo-realistic single image super-resolution using a generative adversarial network. In *International Conference on Computer Vision and Pattern Recognition (CVPR)*, 2017. 2

- [32] V. S. Lempitsky and D. V. Ivanov. Seamless mosaicing of image-based texture maps. In *International Conference on Computer Vision and Pattern Recognition (CVPR)*, 2007. 2
- [33] H. P. A. Lensch, W. Heidrich, and H.-P. Seidel. A silhouette-based algorithm for texture registration and stitching. *Graphical Models*, 63(4):245–262, 2001. 2
- [34] Y. Li, V. Tsiminaki, R. Timofte, M. Pollefeys, and L. V. Gool. 3D appearance super-resolution with deep learning. In *International Conference on Computer Vision and Pattern Recognition (CVPR)*, June 2019. 3
- [35] R. Liao, X. Tao, R. Li, Z. Ma, and J. Jia. Video super-resolution via deep draft-ensemble learning. In *Proc. International Conference on Computer Vision (ICCV)*, 2015. 2
- [36] C. Liu. *Beyond Pixels: Exploring New Representations and Applications for Motion Analysis*. PhD thesis, Massachusetts Institute of Technology, 2009. 5
- [37] C. Liu and D. Sun. On bayesian adaptive video super resolution. *IEEE Transactions on Pattern Analysis and Machine Intelligence*, 36(2):346–360, 2014. 2
- [38] R. Maier, K. Kim, D. Cremers, J. Kautz, and M. Nießner. Intrinsic3D: High-Quality 3D Reconstruction by Joint Appearance and Geometry Optimization with Spatially-Varying Lighting. In *Proc. International Conference on Computer Vision (ICCV)*, 2017. 2
- [39] D. Mitzel, T. Pock, T. Schoenemann, and D. Cremers. Video super resolution using duality based TV-L1 optical flow. In *Pattern Recognition (Proc. DAGM)*, 2009. 2
- [40] C. Nhan Duong, K. Luu, K. Gia Quach, and T. D. Bui. Beyond principal components: Deep boltzmann machines for face modeling. In *International Conference on Computer Vision and Pattern Recognition (CVPR)*, 2015. 3
- [41] K. Olszewski, Z. Li, C. Yang, Y. Zhou, R. Yu, Z. Huang, S. Xiang, S. Saito, P. Kohli, and H. Li. Realistic dynamic facial textures from a single image using gans. In *Proc. International Conference on Computer Vision (ICCV)*, 2017. 3
- [42] S. Park, H. Son, S. Cho, K. Hong, and S. Lee. SRFeat: Single image super-resolution with feature discrimination. In *European Conference on Computer Vision (ECCV)*, 2018. 2
- [43] M. Ranzato, F. J. Huang, Y. Boureau, and Y. LeCun. Unsupervised learning of invariant feature hierarchies with applications to object recognition. In *International Conference on Computer Vision and Pattern Recognition (CVPR)*, 2007. 3
- [44] G. Riegler, M. Rüther, and H. Bischof. ATGV-Net: Accurate depth super-resolution. In *European Conference on Computer Vision (ECCV)*, 2016. 4
- [45] S. Saito, L. Wei, L. Hu, K. Nagano, and H. Li. Photorealistic facial texture inference using deep neural networks. In *International Conference on Computer Vision and Pattern Recognition (CVPR)*, 2017. 2
- [46] M. S. M. Sajjadi, B. Schölkopf, and M. Hirsch. Enhancenet: Single image super-resolution through automated texture synthesis. In *Proc. International Conference on Computer Vision (ICCV)*, 2017. 2
- [47] M. S. M. Sajjadi, R. Vemulapalli, and M. Brown. Frame-recurrent video super-resolution. In *International Conference on Computer Vision and Pattern Recognition (CVPR)*, 2018. 2
- [48] J. Salvador and E. Prez-Pellitero. Naive bayes super-resolution forest. In *Proc. International Conference on Computer Vision (ICCV)*, 2015. 2
- [49] A. Shocher, N. Cohen, and M. Irani. "Zero-Shot" super-resolution using deep internal learning. In *International Conference on Computer Vision and Pattern Recognition (CVPR)*, 2018. 2
- [50] T. Takai, A. Hilton, and T. Mastuyama. Harmonised texture mapping. In *International Symposium on 3D Data Processing Visualization and Transmission (3DPVT)*, 2010. 2
- [51] X. Tao, H. Gao, R. Liao, J. Wang, and J. Jia. Detail-revealing deep video super-resolution. In *Proc. International Conference on Computer Vision (ICCV)*, 2017. 2
- [52] C. Theobalt, N. Ahmed, H. P. A. Lensch, M. A. Magnor, and H.-P. Seidel. Seeing people in different light-joint shape, motion, and reflectance capture. *IEEE Transactions on Visualization and Computer Graphics*, 13(4):663–674, 2007. 2
- [53] R. Timofte, V. D. Smet, and L. V. Gool. Anchored neighborhood regression for fast example-based super-resolution. In *Proc. International Conference on Computer Vision (ICCV)*, 2013. 2
- [54] R. Timofte, V. D. Smet, and L. V. Gool. A+: Adjusted anchored neighborhood regression for fast super-resolution. In *Asian Conference on Computer Vision (ACCV)*, 2014. 2
- [55] V. Tsiminaki, J. Franco, and E. Boyer. High resolution 3D shape texture from multiple videos. In *International Conference on Computer Vision and Pattern Recognition (CVPR)*, 2014. 1, 2, 3, 5, 6, 7, 8
- [56] M. Unger, T. Pock, M. Werlberger, and H. Bischof. A convex approach for variational super-resolution. In *Pattern Recognition (Proc. DAGM)*, 2010. 2
- [57] C. Vogel and T. Pock. A primal dual network for low-level vision problems. In *German Conference on Pattern Recognition (GCPR)*, 2017. 4
- [58] M. Waechter, N. Moehrl, and M. Goesele. Let there be color! Large-scale texturing of 3D reconstructions. In *European Conference on Computer Vision (ECCV)*, 2014. 1, 2, 3, 6, 8
- [59] X. Wang, K. Yu, C. Dong, X. Tang, and C. C. Loy. Deep network interpolation for continuous imagery effect transition. In *International Conference on Computer Vision and Pattern Recognition (CVPR)*, 2019. 2
- [60] X. Wang, K. Yu, S. Wu, J. Gu, Y. Liu, C. Dong, Y. Qiao, and C. C. Loy. ESRGAN: Enhanced super-resolution generative adversarial networks. In *European Conference on Computer Vision (ECCV) Workshops*, 2018. 2
- [61] Y. Wang, F. Perazzi, B. McWilliams, A. Sorkine-Hornung, O. Sorkine-Hornung, and C. Schroers. A fully progressive approach to single-image super-resolution. In *International Conference on Computer Vision and Pattern Recognition (CVPR) Workshops*, 2018. 2
- [62] Z. Wang, J. Chen, Steven, and C. Hoi. Deep learning for image super-resolution: A survey. *CoRR*, abs/1902.06068, 2019. 2
- [63] S. Xie, R. Girshick, P. Dollár, Z. Tu, and K. He. Aggregated residual transformations for deep neural networks. In *International Conference on Computer Vision and Pattern Recognition (CVPR)*, 2017. 4

- [64] J. Yamanaka, S. Kuwashima, and T. Kurita. Fast and accurate image super resolution by deep CNN with skip connection and network in network. In *International Conference on Neural Information Processing (ICONIP)*, 2017. 2
- [65] W. Yang, X. Zhang, Y. Tian, W. Wang, and J. Xue. Deep learning for single image super-resolution: A brief review. *CoRR*, abs/1808.03344, 2018. 2
- [66] Y. Zhang, Y. Tian, Y. Kong, B. Zhong, and Y. Fu. Residual dense network for image super-resolution. In *International Conference on Computer Vision and Pattern Recognition (CVPR)*, 2018. 2